Nuclear Materials and Energy 44 (2025) 101968

Contents lists available at ScienceDirect

Nuclear Materials and Energy

journal homepage: www.elsevier.com/locate/nme

Preparing LIBS for in-situ measurements in JET tokamak: system overview and co-deposited layer thicknesses

Jasper Ristkok [a,*], Salvatore Almaviva [b], Jari Likonen [c], Juuso Karhunen [c], Indrek Jõgi [a], Peeter Paris [a], Shweta Soni [d], Pavel Veis [d], Sahithya Atikukke [e], Jelena Butikova [f], Rongxing Yi [g], Ionut Jepu [h], Pawel Gasior [i], Corneliu Porosnicu [j], Mihaela Bojan [j], Bianca Solomonea [j], Sebastijan Brezinsek [g]

[a] Institute of Physics, University of Tartu, Tartu 50411, Estonia
[b] ENEA, Frascati Research Center, via Enrico Fermi, 45, I-00044 Frascati, Italy
[c] VTT Technical Research Centre of Finland, P.O. Box 1000, Espoo 02044 VTT, Finland
[d] Department of Experimental Physics, FMPI, Comenius University, Mlynská dolina F2, 842 48 Bratislava, Slovakia
[e] Department of Astronomy, Physics of the Earth, and Meteorology, FMPI, Comenius University, Mlynská dolina F2, 842 48 Bratislava, Slovakia
[f] Institute of Solid State Physics, University of Latvia, Riga LV-1063, Latvia
[g] Forschungszentrum Jülich GmbH, IFN-1 Plasmaphysics, Jülich, Germany
[h] United Kingdom Atomic Energy Authority, Culham Centre for Fusion Energy, Culham Science Centre, Abingdon, OXON OX14 3DB, United Kingdom
[i] IPPLM Institute of Plasma Physics and Laser Microfusion, Hery Street 23, 01-497 Warsaw, Poland
[j] National Institute for Lasers, Plasma and Radiation Physics, 77125 Magurele, Bucharest, Romania

ARTICLE INFO

Keywords:
LIBS
SIMS
Depth profiles
JET-ILW
Plasma-facing components
Be coatings
Material deposition
Plasma-wall Interaction

ABSTRACT

Laser-induced breakdown spectroscopy (LIBS) is a method for elemental composition analysis that has been proposed for fusion reactor safety diagnostics. A significant milestone in this development was the LIBS campaign conducted in 2024 at the Joint European Torus (JET), using a prototype LIBS enclosure, deployed with the MASCOT tele-manipulation arm. The work presented here prepared for the JET campaign by testing the LIBS enclosure.

Experiments were conducted at VTT Technical Research Centre of Finland, analyzing JET wall samples from the 2011–2016 ILW1–3 fusion campaigns, primarily from the divertor. The focus was on the analysis of co-deposited layers on the plasma-facing components containing hydrogen isotopes and elements from bulk layers: Be, W, Mo, CFC, and Inconel. Measurements were performed under atmospheric pressure air with an argon flow.

Optimal experimental conditions for the use of an Echelle spectrometer in subsequent JET LIBS campaign were identified, and the depth profiles of the surface layers are presented. The LIBS depth profiles defined distinct material layers. Ablating through the co-deposited layers required 1–870 laser shots (~0.1–90 μm) on samples from different locations, with typical variations of 10–40 % on the same sample and the largest variation spanning 15–480 shots (~1.5–50 μm).

The LIBS, Secondary Ion Mass Spectrometry (SIMS), and optical profilometry results showed good qualitative agreement. The ablation rate was ~30–50 nm/shot for the W layers, ~100–140 nm/shot for bulk Be limiters, and intermediate for the co-deposited layers. The insights gained in this study supported the preparation of the JET LIBS campaign.

1. Introduction

International Thermonuclear Experimental Reactor (ITER) is the next-generation fusion device, which is being constructed in Cadarache, France, as an important step in the development of fusion energy. It will use deuterium–tritium fuel and is designed to achieve a Q value of 10 [1]. However, fusion plasma is known to interact with the reactor walls, resulting in erosion of the material and its re-deposition, along with the

* Corresponding author.
E-mail address: jasper.ristkok@ut.ee (J. Ristkok).

https://doi.org/10.1016/j.nme.2025.101968
Received 14 April 2025; Received in revised form 27 June 2025; Accepted 9 July 2025
Available online 10 July 2025

fuel, in other parts of the reactor [2,3]. Tritium is radioactive, and safety regulations limit its retention on the ITER reactor walls to only 700 g [4]. Therefore, an *in-situ* method for monitoring fuel retention is required.

Laser-induced breakdown spectroscopy (LIBS) [5] is considered among the few suitable methods for measuring fuel retention under fusion reactor conditions [6,7,8]. LIBS uses a short, intense laser pulse focused on the target, with the fluence typically being on the order of 1–100 J/cm^2. A small amount of material is ablated, forming a plasma plume that emits light characterizing the ablated material. By recording the emission spectrum, the elemental concentrations of the materials can be determined, either through previous calibrations or by calibration-free LIBS (CF-LIBS) [9,10].

LIBS offers several advantages: it is fast, relatively non-invasive, capable of detecting all elements, and operable from a distance. However, it also has limitations. LIBS ablates and excites only a small amount of the material, limiting the signal intensity. Furthermore, overlapping emission lines can complicate the distinction of different elements. Additional restrictions of LIBS systems are caused by the harsh radioactive environment of fusion reactors that allows direct LIBS recordings only from a distance which results in significant signal losses. Moreover, not all areas in the vacuum vessel are accessible to the laser beam [11]. One option is to use a compact LIBS measuring head which can be manipulated and moved inside of the tokamak with robotic arm [11,12]. Delivering sufficient laser radiation through the fiber is very challenging [11], but having a built-in laser in the LIBS measuring head sets limits to the laser dimensions and weight [13]. In both cases, delivering laser-induced plasma radiation through a long fiber attenuates the LIBS signal, especially in the UV region. Consequently, LIBS must be tested and optimized for fusion reactor applications.

While *in-situ* LIBS has already been used in tokamaks [11,12,14,15], the decommissioning of JET provided a unique opportunity to test *in-situ* LIBS with fusion reactor samples containing tritium. Tritium has been previously recorded with LIBS [8] in laboratory conditions from specially produced metallic films and at lower pressure in tritium-enriched zircaloy tubes [16]. The 2024 LIBS campaign in JET was designed to pave the way for using LIBS in ITER and other future fusion reactors for fuel retention and material migration measurements. Additionally, the campaign would evaluate the performance of an improvement to the LIBS enclosure used in the Frascati Tokamak Upgrade (FTU) [14], during *in-situ* experiments. The 2024 JET LIBS campaign marked the first use of the compact LIBS system, using a robotic arm, to conduct measurements under atmospheric pressure in JET containing tritium and beryllium.

A measurement campaign at the beryllium- and tritium-compatible facilities of VTT Technical Research Centre of Finland was conducted as a preparation for the LIBS campaign at JET, utilizing a newly built experimental setup mimicking the JET measurements in laboratory conditions. The goal was to test the compact LIBS system to study its limitations: how the system operates with the lightweight laser with limited energy, what are the limitations of a 20-meter optical fiber, and how the use of atmospheric pressure argon flow influences the results. It was necessary to identify optimal experimental parameters for JET and rehearse the operation of the system due to the limited experimental time there. Specifically, the VTT measurements aimed to optimize camera settings, such as delay time, for the broad wavelength range Echelle spectrometer useful for measurements of elemental composition of the layers, and to examine depth profiles of the samples originating from JET 2011–2016 ILW1–3 fusion campaigns [2]. These samples had similar properties to the current JET reactor plasma-facing components, also containing Be deposits, which made it possible to determine the number of shots required to ablate through the co-deposited layers. The LIBS results were compared with secondary ion mass spectrometry (SIMS) depth profiles for cross-checking, and optical profilometry was used to estimate the laser ablation rates for the co-deposited layers. Quantitative measurement of fuel retention by CF-LIBS was planned for the JET campaign but is not used in this study due to the main emphasis being on testing the prototype and finding the depth profiles. For the same reason, electron density and temperature are not analyzed in this paper.

2. Methods

2.1. Experimental setup

In the experiments performed at JET, the LIBS system was mounted on the remotely controlled MASCOT robotic arm [17], which could access most of the locations inside the JET vessel. The maximum payload capacity of MASCOT placed constraints on the dimensions and mass of the LIBS enclosure. To address these constraints, and to protect the electronics of the spectrometer and the ICCD detector, the spectra-recording equipment was separated from the LIBS enclosure via a 20-meter optical fiber. The resulting LIBS enclosure, constructed at the National Laboratory of Frascati in Italy, represents a further development of the one used in FTU [13,14]. The prototype LIBS system is shown in Fig. 1, and it contained a lightweight laser, optics, and an argon-flow tube.

The enclosure contained a Montfort Laser M−Nano Nd:YAG laser, operating at a wavelength of 1064 nm, having a pulse duration of 0.8 ± 0.2 ns. Sub-ns laser pulses give smaller ablation rate and result in smaller outgassing [18,19]. The pulse repetition rate of 2 Hz was selected due to the limitations set by the camera of the spectrometer. The laser beam had a Gaussian profile with approximately 20 % modulations at the peak, and the resulting crater was ellipsoidal, likely due to the slight misalignment of the optics, with the major and minor axes being 0.6 mm and 0.4 mm, respectively. Requirement of the use of a compact laser imposed limitations on the maximum output energy, and the maximum pulse energy of 10 mJ was used for a sufficiently strong LIBS signal. The pulse energy at the target was reduced to 8 mJ due to losses in the optical system. Therefore, the resulting fluence was 4 J/cm^2 and irradiance of power density was 5 GW/cm^2.

The laser beam was guided using three lenses and two mirrors (Fig. 1): lens 1 (1″ diameter, f = -75 mm, IR/AR coated), lens 2 (2″ diameter UVFS, f = 200 mm, IR/AR coated), mirror 1 (1″ diameter, HR-IR 45° Nd:YAG mirror, IR/AR coated), mirror 2 (2″ diameter, HR-IR HT-VIS 45° dielectric mirror – Standa 14DM-2-HR14-45–2), and lens 3 (2″ diameter UVFS, f = 75 mm, IR/AR coated). Mirror 2 was a dielectric 1064 nm laser line mirror, which has transparency in the visible and UV part of the spectrum with some stronger absorption regions. The laser beam was focused by lens 3 a few millimeters inside the target to prevent breakdown of the background gas. The experiments were conducted in atmospheric pressure air with an argon flow of 1 slm with purity of 99.999 % to prolong the LIBS signal [20] and to protect the target from oxidation during measurements. The target was positioned against a cone, which was used to facilitate argon as the background gas and to ensure repeatable focusing of the optical setup. The measurement series began only after the argon had flowed for a minute to remove most of the air from the cone. Due to the beryllium content and trace amounts of tritium in the samples, the LIBS system and samples were housed in a fume cupboard. To limit the contamination of the LIBS system, the samples were enclosed in a secondary Plexiglass cabinet with a hole for the cone. The samples were fixed to an x-y translational holder, allowing accurate adjustment of the laser beam position on the sample surface. The distance between the craters was set to 1 mm.

The plasma plume emission was collected collinearly, perpendicular to the target surface, through lens 3 and mirror 2, and then focused with lens 4 (2″ diameter UVFS Plano convex lens, f = 75 mm) onto a 20-meter optical fiber with a 1.6 mm diameter. The field of view of the fiber was 3.35 mm on the target surface. This resulted in the collection of the emission from the entire plasma plume with an expected size of 1–3 mm at atmospheric pressure [21,22]. The fiber was split into seven outputs to facilitate multiple spectrometers and other diagnostic tools at JET.

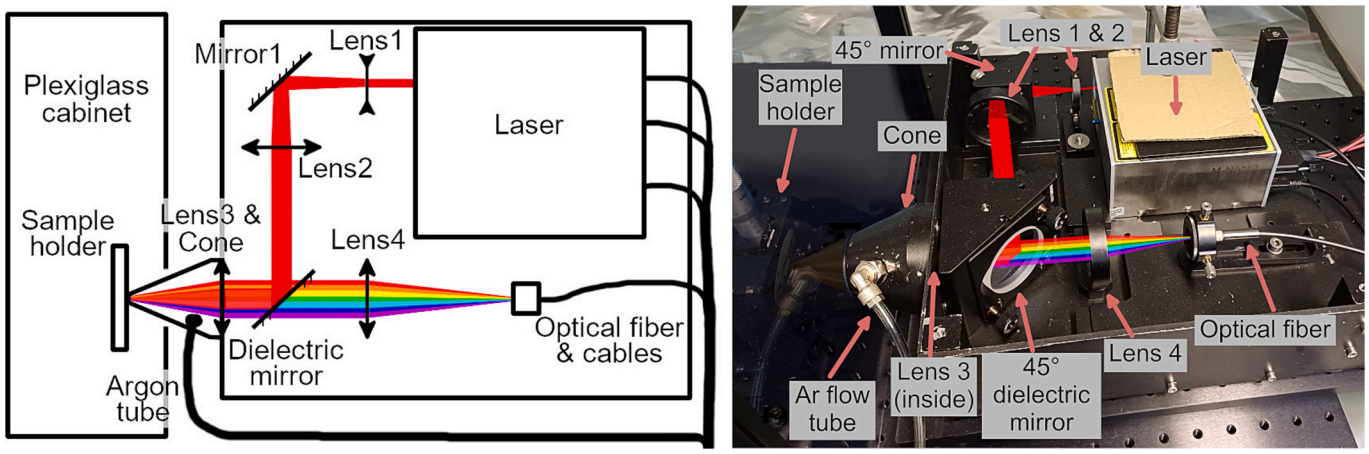

Fig. 1. The schematic on the left and photo on the right of the compact LIBS enclosure without the top cover. This is the prototype of the unit that was moved around in JET with the robotic arm. The cone is pressed against the sample with argon flow replacing air inside the cone. Emitted light is collected into a 20-meter fiber and transmitted to the Aryelle spectrometer coupled with an ICCD camera.

These were situated outside of the LIBS enclosure.

One of the fiber outputs was connected to a wide spectral range Echelle-type spectrometer for detecting elements in the samples. Another output was designated for a high-resolution Littrow spectrometer, operated at different camera settings, capable of distinguishing the spectral lines of different hydrogen isotopes at around 656 nm. However, the Littrow spectrometer was not used during the VTT LIBS campaign and thus, won't be discussed in this paper.

For wide-spectral-range measurements, an Aryelle 200 spectrometer from LTB Lasertechnik Berlin GmbH was used along with an LTB Hg calibration lamp (standard S/N:127/1.0/23) provided with the spectrometer. The apparatus function of the spectrometer, based on the full widths at half maximum (FWHM) of the Hg spectral lines, was 0.03 nm at the 250 nm region and increased to 0.07 nm at 600 nm. The Aryelle spectrometer was coupled with an Andor iStar DH334T-18U-E3 ICCD camera. To determine optimal acquisition parameters for *in-situ* measurements at JET, the camera gate width and delay time were varied between 500–5000 ns and 500–2500 ns, respectively. The depth profiles presented in this paper were obtained with both the gate width and delay time set to 1000 ns.

Wavelength correction of the spectra was performed using the Hg calibration lamp, achieving an accuracy of a few picometers within the 200–760 nm spectral window. The spectral sensitivity calibration was done using an Ocean Optics DH2000 deuterium-halogen lamp, and the intensity was corrected with the camera gain function and gate width. For both calibrations, the fiber was disconnected from the LIBS enclosure and directly attached to the calibration lamp. Consequently, the sensitivity curve did not account for the optics inside the LIBS enclosure.

Optical profilometry and SIMS were conducted on the samples as a cross-reference for LIBS. Profilometry was performed using an Ambios Xi-100 Non-Contact Optical Profilometer, based on Michelson interferometry, at the National Institute for Laser, Plasma and Radiation Physics in Romania. SIMS analysis was conducted at VTT during 2021–2022 using double-focusing magnetic sector instrument VG Ionex IX-70S. The results of the SIMS measurements have been published in an earlier paper [23].

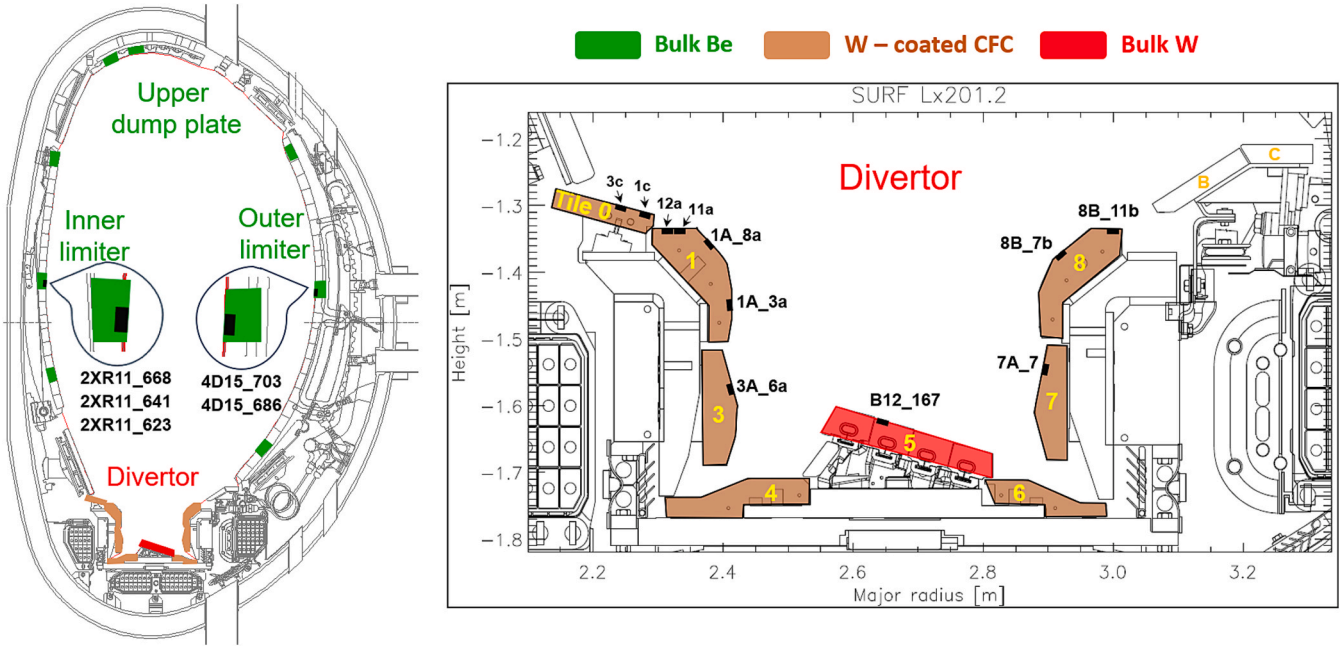

Fig. 2. Studied samples and locations in the JET vessel from which these originated. Note that the Be-coated Inconel sample IWC_2 mimicking the inner vessel wall was also studied, but it was not exposed to JET plasma and was included only for identifying Inconel spectral lines.

2.2. JET samples

Samples from JET limiter and divertor tiles, exposed during the 2011–2016 ILW1–3 campaigns [2], were used in this study (Fig. 2). The aim was to have an overview of the co-deposited layer thicknesses at characteristically different locations within the reactor for the subsequent LIBS campaign in JET. The depth profile of only one sample from each characteristic location is presented in this paper (Table 1). For example, other castellations on the limiter tile 2XR11 produced similar results to castellation 668, which is shown in the paper.

A typical divertor tile consisted of W-coated CFC with a Mo adhesion layer (Fig. 3). The exceptions were tile 5, which consists of bulk W, and the limiter tiles, which consist of bulk Be. The inner vessel wall of JET consists of Be-coated Inconel (Ni, Fe, Cr). A Be-coated Inconel sample IWC_2 was also studied for the Inconel spectral data but is not discussed further in this paper as it was not exposed to JET plasma.

The samples, cut from the JET tiles, varied in size and shape (Fig. 4), but were all at least 1 cm thick, so LIBS thermal effects were negligible. They also displayed significant differences in layer composition, material structure (e.g., porosity and grain size), and co-deposited layer thicknesses, as shown in section 3.4.

3. Results

3.1. Recorded spectra

The spectra were recorded with automatic background correction before every laser shot series. An example of the recorded spectra with the sensitivity curve is shown in Fig. 5. The measured wavelengths ranged from 200 to 760 nm. Due to the characteristics of the Echelle-type spectrometer, spectral sensitivity correction was crucial. For instance, the intensity ratio of the most reliable Be I 457.27 nm and W I 400.88 nm lines changed by a factor of two after applying the sensitivity correction.

Spectral lines were fitted by Fityk software [25] with Voigt profiles, using Levenberg–Marquardt algorithm and the standard rapid approximation of Voigt profile algorithm of Fityk. An example of Voigt fitting of W I 400.88 nm line and Be I 457.27 nm line is shown in Fig. 6. The Gaussian component of the Voigt profile is related to the apparatus function and, for lighter elements such as Be, H, and Ar, to the Doppler broadening. The Lorentzian component of the Voigt profile is related to the Stark broadening, which is also more pronounced for the lighter elements. The fitting process subtracted the local continuum signal, as the continuum intensity varies across the recorded wavelengths [26]. The key extracted parameters for each line were the line intensity (area under the line) and width (FWHM), which are related to plasma temperature and electron density, respectively [9,10]. However, in this study, line width and the plasma parameters are not analyzed.

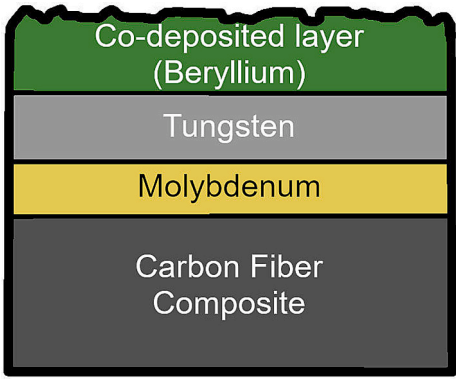

Fig. 3. The composition of a typical W-coated CFC divertor tile.

The calibration lamp spectra revealed significant attenuation of the signal below 270 nm, attributed to the transmission properties of the 20-meter fiber, the spectrometer, and the camera. Additional attenuation regions below 300 nm and around 350–370 nm were observed from the lack of continuum and spectral lines (Fig. 5), likely caused by the LIBS enclosure optics. However, enough spectral lines were present in other wavelength regions, ensuring the attenuation did not have a large impact on the outcomes of the study.

3.2. Identification of spectral lines

The JET samples were expected to contain measurable quantities of the hydrogen isotopes, Be, W, Mo, C, Inconel (Ni, Fe, Cr), and potentially O [2]. The spectral lines were identified using the NIST [27] and Kurucz [28] databases, and by comparing the depth profile of each line to that of known lines, ensuring reliable identification of the lines. If the depth profile of a given line deviated from the depth profile of the goup of identified lines of the same element, then the given line was either misidentified or experienced considerable self-absorption. Be, W, and Mo lines were easily identified from the spectra of the HFGC samples with distinct thick co-deposited, W, Mo, and CFC layers. Ni, Fe, and Cr lines were identified from the clean Inconel sample IWC_2, which had a Be coating mimicking the JET inner wall.

Ar signal was introduced by the background gas. Two Cu I resonance lines at 324.76 and 327.39 nm were present throughout the co-deposited layers, though the origin of Cu remains unclear. Ca II lines at 393.37 and 396.85 nm emerged only as surface contamination. N I lines at 742.36,

Table 1
Overview of LIBS samples presented in this study. More samples were used from different locations but behaved similarly to the ones shown.

Sample name	Location	Bulk layer(s)	Fusion campaigns	Dominant erosion/deposition [2,24]	Co-deposited layer thickness by SIMS, μm
4D15_703	Outer limiter	Be	ILW 1–3	Erosion	–
2ONG8B_11b	Tile 8	CFC, Mo, W	ILW 2–3	Both	0.25*
2ONG7A_7	Tile 7	CFC, Mo, W	ILW 2–3	Both	–
B12_167	Tile 5	W lamella	ILW 1,3	Erosion	0.05
2IWG3A_6a	Tile 3	CFC, Mo, W	ILW 3	Erosion	2.6**
14IWG1A_3a	Tile 1 vertical	CFC, Mo, W	ILW 1–3	Deposition	3.3
14IWG1A_8a	Tile 1 diagonal	CFC, Mo, W	ILW 1–3	Deposition	–
14IWG1A_11a	Tile 1 horizontal	CFC, Mo, W	ILW 1–3	Deposition	31***
HFGC_1c	Tile 0	CFC, Mo, W	ILW 1–3	Deposition	>22****
2XR11_668	Inner limiter	Be	ILW 1–3	Erosion	0.22
IWC_2	Inner Wall Cladding	Be coating, Inconel (Ni, Fe, Cr)	Not exposed	Not exposed	–

* SIMS was done on a nearby sample 2ONG8B_10a.
** SIMS was done on a nearby sample 2IWG3A_6b. Layer is defined by falling Be signal for SIMS-LIBS comparison.
*** SIMS was done on a nearby sample 14IWG1A_10a.
**** Not enough SIMS data to penetrate into the W layer.

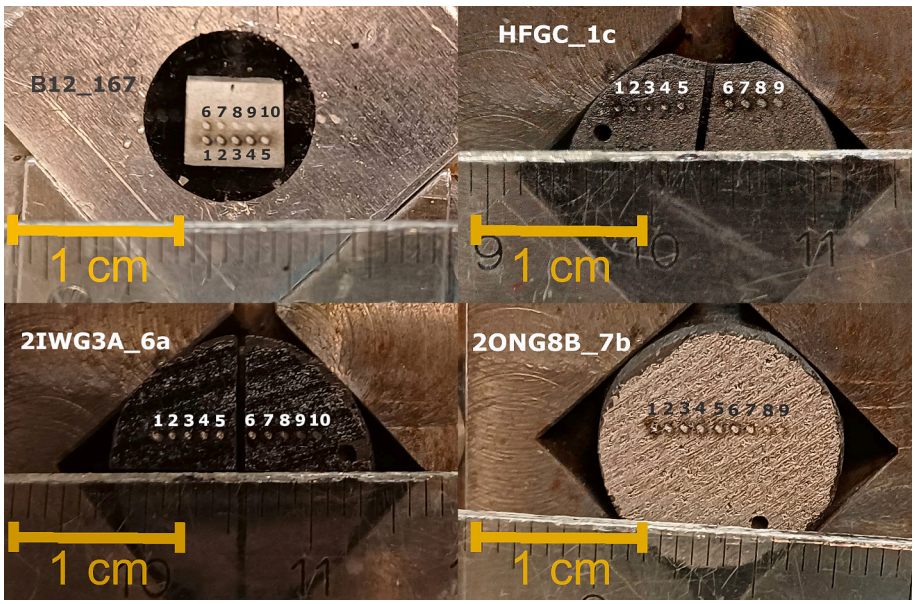

Fig. 4. Examples of different samples after the LIBS experiments. The samples varied significantly in elemental composition, bulk material properties, and co-deposited layer structure. Spots 1–5 were analyzed using different delay times, while spots 6 + were created for profilometry measurements.

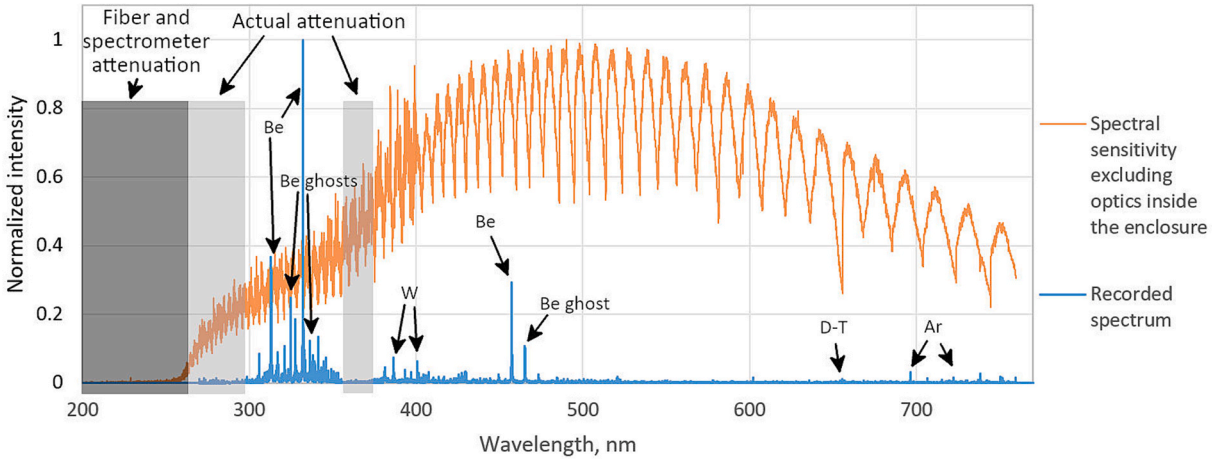

Fig. 5. An example of the recorded spectrum of the 2IWG3A_6a JET sample on the 3rd shot at 1 μs delay time, shown in blue. There is signal attenuation below 300 nm and around 350–370 nm. Some of the strongest lines of different elements have been shown. The spectral sensitivity curve determined from halogen and deuterium calibration lamp outputs, excluding the LIBS enclosure optics, is shown in orange. The actual attenuation is also determined by the transmission properties of the LIBS enclosure optics, such as the dielectric mirror. The sensitivity modulation arises from the way the Aryelle spectrometer compiles the spectrum. (For interpretation of the references to colour in this figure legend, the reader is referred to the web version of this article.)

744.23, and 746.84 nm most likely from ambient air were mainly at the noise level but were detectable at 500 ns delay times. C and O lines were not detected in the recorded spectra, although the C II 426.73 nm line has been observed previously at lower pressure [29]. The strongest lines of O, N, and C fell outside the measured spectral region (O I 777.19, 777,42 and 777,54 nm, N I 174.27 and 868.03 nm, and C I 165.70 and 193.09 nm lines), while the prominent C I 247.86 nm line was in the attenuation region of the optics. Future studies of the application of LIBS on the remote arm of fusion reactors where boron is present on the surface of the first wall [30] may face similar challenges, as the strongest B I lines lie at 249.68 and 249.77 nm and below 200 nm.

In total, 370 spectral lines were detected, with 160 having line amplitude at least three times above the noise level. Of these, only 60 were reliable and usable for LIBS analysis, as many lines were interfered by unidentified lines or the lines of other elements. The reliable spectral lines of neutrals, also considering self-absorption effects, are summarized in Table 2. Other lines either were not detected, had clearly different depth profiles (could not be identified or were self-absorbed), or were interfered by some other line nearby.

The strong broadening of the H_α 656.28 nm and D_α 656.10 nm lines at atmospheric pressure and used delay times made it impossible to separate them. During the JET LIBS campaign, an additional Littrow spectrometer with alternative camera settings and higher spectral resolution addressed this issue.

There were indicators of strong self-absorption of the Be I 332.13 nm line and the overlapping Be II lines at 313.04 and 313.11 nm, making the intensity of these lines unreliable. The indicators included a distinctly slower decrease of peak amplitude over subsequent shots, compared to other lines in the spectra, and an evident line reversal in the peak of the Be II overlapping lines. Closer inspection revealed a dip in the peak at the location of both Be II lines. The persistent intensity could give a false impression that Be was deep within the bulk material when, in reality, self-absorption and ablation from the crater sides (discussed in section 3.4) were influencing the measurements.

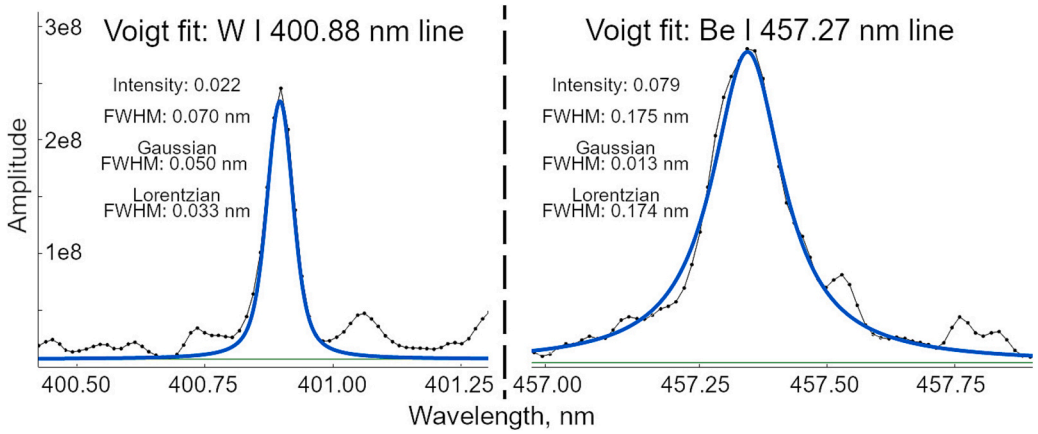

Fig. 6. An example of the Voigt fitting for sample HFGC_1c shot 800 at 1 μs delay time with W I 400.88 nm line and Be I 457.27 nm line. The shape of Be, H and Ar lines was dominated by Lorentzian, and the shape of W, Mo and Inconel lines was dominated by Gaussian. The intensities are normalized in accordance with section 3.4.

Table 2
Reliable lines of neutrals identified for each detected element. Note that there was no signal below 300 nm, over 760 nm and around 360 nm. The Be I 332.13 nm line was self-absorbed based on the different shape of its depth profile and persisting intensity of the line, but could be considered more reliable than the Be II 313.04–313.11 nm overlapping lines.

Element	Wavelengths (nm)
H_α/D_α	656.28/656.10
H_α/D_α	656.28/656.10
Be I	381.35, 457.27
Ar I	696.54, 706.72, 738.44, 750.39, 751.53
W I	321.56, 400.88, 407.44, 429.46, 430.21
Mo I	319.40, 379.83, 386.41, 390.30, 418.83, 550.65, 553.30, 557.04
Ni I	300.25, 301.20, 305.08, 310.16, 338.06, 341.48, 342.38, 344.63, 345.85, 346.17, 349.30, 351.04, 351.51, 352.45
Cr I	425.43, 428.97, 520.45, 520.60, 520.84
Fe I	344.06, 371.99, 373.49, 373.71, 374.56, 374.83, 374.95, 375.82, 382.04, 385.99, 388.63, 404.58, 438.36
N I	742.37, 744.23, 746.83

One issue encountered was crosstalk – the appearance of "ghost lines" which are artifacts caused during the process of compiling the spectrum in an Echelle-type spectrometer. If a spectral line has high intensity, then the light from spectrometer output will appear on adjacent diffraction orders on the camera matrix, resulting in a weaker but distinct line appearing in the spectrum where nearby diffraction orders are inserted (Fig. 5). The ghost lines were usually on both sides of a nearby strong line and had comparable FWHM with the real line, making them easier to identify. In this case, the ghost lines at higher wavelengths had higher intensity than the ghost lines at lower wavelengths, suggesting non-ideal alignment in spectrometer calibration. The spectra contained ghost lines next to the overlapping Be II lines at 313.04–313.11 nm (ghost lines at four locations: 305.9, 309.4, 316.8, 320.7 nm), Be I line at 332.13 nm (324.3, 328.1, 336.4, 340.8 nm), Be I line at 457.27 nm (449.7, 465.4 nm), and next to Ca II line at 396.85 nm (399.4 nm).

Only a few ionic lines were observed in the spectra, notably the prominent W II ionic lines (e.g. 302.45 and 334.31 nm) and the aforementioned Be II and Cu II lines. No other ionic lines of other elements, including the Be II line at 467.34 nm, were identified. This was likely due to the use of a shorter laser pulse than previously [29], which results in lower electron temperature in the plasma plume, and due to the use of atmospheric pressure, which expectedly results in rapid quenching of higher-energy states.

3.3. Delay time optimization

The LIBS measurements were conducted for each sample using varying delay times between the laser shot and the recording of the spectrum. The aim was to determine the optimal delay time to use during the JET LIBS campaign. Delay times of 500, 1000, 1500, 2000, and 2500 ns were tested, with a constant gate width of 1000 ns. The gate width was chosen as a compromise between signal intensity and temporal resolution, the latter being critical for the planned use of CF-LIBS for fuel retention measurements in JET campaign. A new spot on the sample was used for each delay time (craters 1–5, Fig. 4).

The determination of the optimal delay time was somewhat inconclusive, as each delay time had distinct advantages and disadvantages. At delay times above 1500 ns and with gate widths below 1000 ns, the signal-to-noise ratio became undesirably poor for our setup, as the signal intensity drops with delay time [20]. At shorter delay times, particularly at 500 ns, Be, N, and Ar lines appeared asymmetrical. This asymmetry during the early stages of the plasma plume life can be explained by the Stark shift, which is determined by electron density [31]. Fitting these asymmetrical lines with a single profile (Gaussian, Lorentzian, or Voigt) introduces errors in the extracted line parameters. On the one hand, longer delay times result in relatively slow changes in plasma parameters, which is advantageous for CF-LIBS applications [32]. On the other hand, at longer delay times, the lower electron density is an issue for CF-LIBS because the local thermodynamic equilibrium conditions might not be fulfilled [21,32]. Ultimately, the gate width and delay time of 1 μs were selected as a compromise for the JET LIBS campaign.

3.4. Comparison of LIBS and SIMS depth profiles

Samples from various parts of JET divertor and limiters (Fig. 2, Table 1) were analyzed to provide an overview of the thickness of the co-deposited layers throughout the reactor. The depth profiles of JET ILW 1 inner divertor tiles have been studied previously, albeit with a different material composition [29]. To estimate the number of laser shots required to ablate through the co-deposited layer and to assess the time needed for such an endeavor during the JET LIBS campaign, hundreds to thousands of shots were recorded in each crater. All LIBS results presented in this section were obtained with a 1 μs delay time.

For clarity, only the line intensities of the five prominent elements are shown in the depth profiles. Ni was selected to represent Inconel, while Fe and Cr were excluded due to the similarity of their depth profiles to that of Ni. The Ar signal remained relatively constant throughout the depth and was thus also omitted. One should consider that the trace amount of remaining air, and the 656.32 nm W I line could

have added some signal to the line of hydrogen isotopes.

To construct the LIBS depth profiles, the intensities of all reliable lines for each element (Table 2) were summed (Eq. (1)) to improve the signal-to-noise ratio. Despite this, the summed intensities exhibited significant fluctuations. To address this, a moving median with replication padding for the first and last shots (Eq. (2)) was used instead of a moving average, which was overly influenced by large outliers. This approach allowed the creation of reasonably smooth depth profiles, with distinct sample layers becoming evident. All of the presented depth profiles are max-normalized (Eq. (3)) as a group (LIBS and SIMS separately), meaning the intensities of different samples can be compared. Following formula were used in the process:

$$S_{i,k} = \sum_{j=1}^{n_i} I_{jk} \tag{1}$$

$$M_{i,k} = \mathbf{median}\left(S_{i,k-r}, \cdots, S_{i,k+r}\right);\ \ \boldsymbol{clip}\left(x\ \boldsymbol{in}\ S_{i,x}\ \boldsymbol{between}\ 0\ \boldsymbol{and}\ k_{max}\right) \tag{2}$$

$$N_{i,k} = \frac{M_{i,k}}{S_{max}};\ \ S_{max} = \boldsymbol{max}_{i,k}\left(M_{i,k}\right), \tag{3}$$

where I is the intensity of one spectral line, S is the sum of intensities, index i represents an element, index k represents the shot number, index j represents the line index and n is the amount of spectral lines for the respective element; M is the median of the intensity at a given shot, r is the radius of the moving median and index x is any index within range; S_{max} is the maximum intensity of the moving medians and N is the normalized moving median value at a given shot.

The Gaussian laser beam, which ablates the crater center as well as the sides, can result in surface layer signals persisting even after the center of the beam reaches the next layer [33]. Therefore, the LIBS shot corresponding to ablating through the co-deposited layer was defined as the point where the bottom layer signal reached 50 % of its maximum on the rising edge. For samples where only a falling edge was present, the same 50 % criterion was applied to the falling edge instead.

Main net erosion regions – limiters and tile 5

The samples of W lamella from tile 5 stack B (Fig. 7a and Fig. 7b), and inner (Fig. 7c) and outer wall Be limiters produced similar results: the co-deposited layer was ablated with just 1–2 laser shots and afterwards the signals remained nearly constant. This supports the expectations that these surfaces are relatively clean due to minimal deposition and significant erosion. LIBS and SIMS agreed on the primary elements in the co-deposited and bulk layers. For the limiter tile, the SIMS depth profile lacked distinct features, similarly to Fig. 7a.

For the tile 5 sample, ablation through the co-deposited layer was estimated by the falling signal of Be. For the bulk Be limiter tiles, ablation through the co-deposited layer was estimated by the fall of the signal of other deposited elements (Inconel, W, Mo). Note that the measurements of the different samples on the limiter tiles did not include the two castellation columns nearest to the edge, where the co-deposited layer might be thicker due to shadowing effects [34].

Thickest co-deposited layer: tile 0

The HFGC_1c sample contained three bulk layers: W, Mo, and C (Fig. 7d) and represents a typical W-coated CFC (Fig. 3). While C was not detected (sections 3.1 and 3.2), the boundary of the CFC layer could be estimated from the decreasing Mo signal. This sample had the thickest co-deposited layer, requiring 600–870 shots to ablate through.

The first 300 shots from this sample were also used to analyze shot-to-shot and crater-to-crater signal variation and layer thickness variation across craters separated by a few millimeters (discussed in section 3.6). SIMS measurements for this sample reached only 22 μm in depth, insufficient to penetrate into the W layer. Consequently, the SIMS depth profile lacked distinct features, similarly to Fig. 7a, and is not shown.

Co-deposited layer thickness gradient: tile 1

These samples characterize the gradient in co-deposited layer thickness moving vertically in the inner divertor. Tile 1 comprises vertical, diagonal, and horizontal sections (Fig. 2). Similarly to tile 0, the bulk was W-coated CFC (Fig. 8). Sample 14IWG1A_3a from the vertical part of tile 1 required around 40 laser shots to ablate through the co-

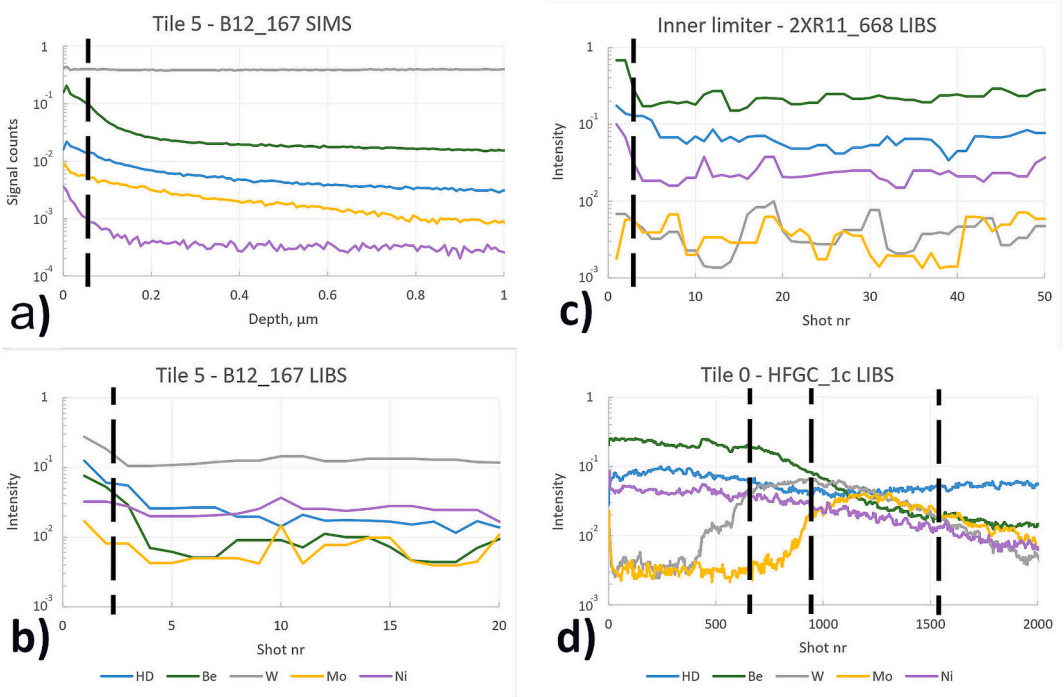

Fig. 7. The depth profiles of a) SIMS and b) LIBS for tile 5 sample B12_167. The LIBS depth profiles of c) inner limiter sample 2XR11_668 and d) tile 0 sample HFGC_1c. LIBS data is smoothed with a moving median over b) 3, c) 3, d) 21 shots for improved visualization. There is a clear distinction between the co-deposited layer, W-layer, and Mo-layer with the tile 0 sample.

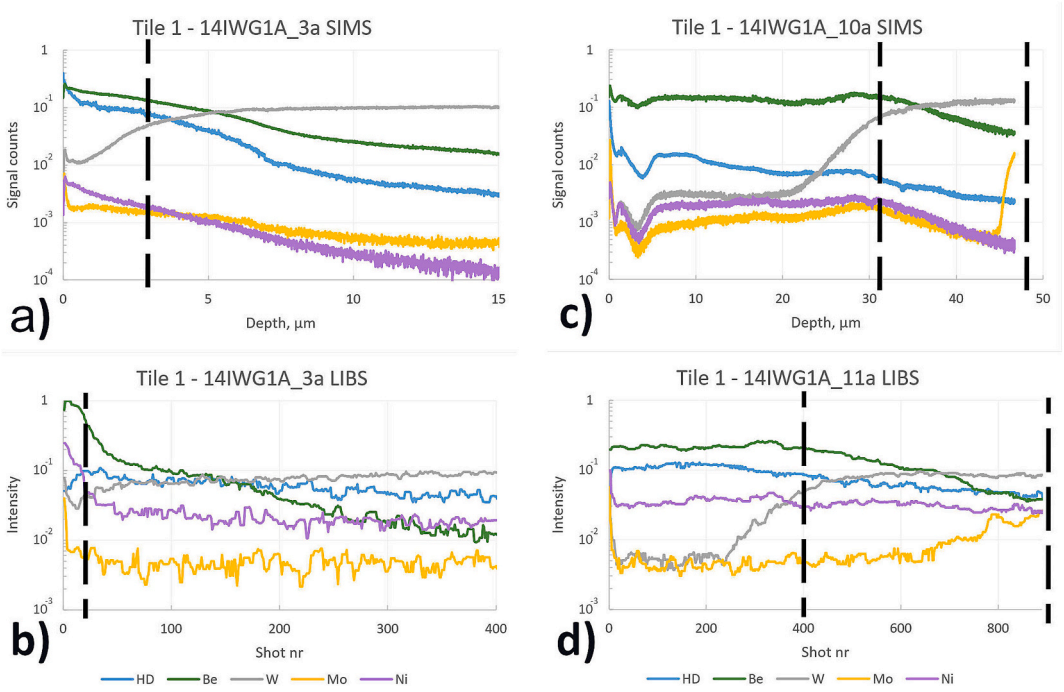

Fig. 8. The depth profiles of a) SIMS and b) LIBS for tile 1 sample 14IWG1A_3a. The depth profiles of a) SIMS and b) LIBS for tile 1 sample 14IWG1A_11a and nearby sample 14IWG1A_10a. LIBS data is smoothed with a moving median over b) 7, d) 21 shots for improved visualization.

deposited layer, while sample 14IWG1A_11a ("the apron") from the horizontal part required 15–480 shots, depending on the location on the sample, with the median being 120 laser shots.

For the sample 14IWG1A_3a, the LIBS and SIMS depth profiles showed qualitative agreement, as seen in Fig. 8a and Fig. 8b. The only notable discrepancy was in the profile of the hydrogen isotopes. LIBS detected an initial increase in the hydrogen isotopes signal, which then plateaued. In contrast, SIMS showed a continuous decrease in the hydrogen isotopes signal with depth. This divergence may be attributed to changing LIBS plasma parameters after the initial shots and at the transition to the W layer. This explanation also applies to other depth profile comparisons.

For the sample 14IWG1A_11a, the LIBS and SIMS depth profiles were similar, as shown in Fig. 8c and Fig. 8d. SIMS data was available only for

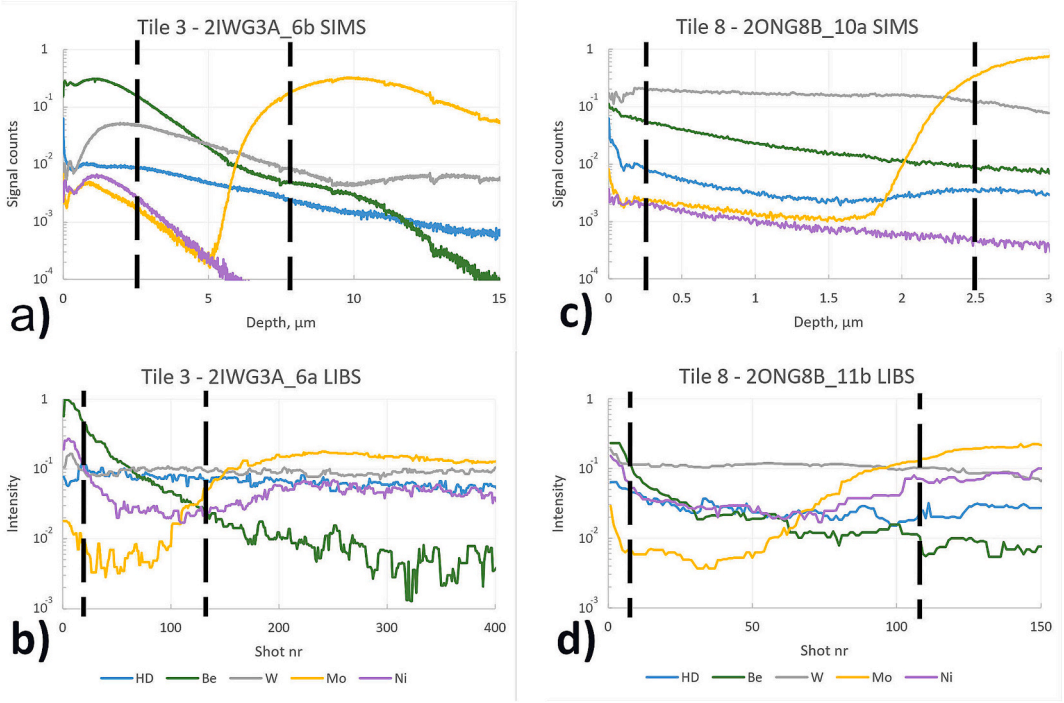

Fig. 9. The depth profiles of a) SIMS and b) LIBS for tile 3 sample 2IWG3A_6a and nearby sample 2IWG3A_6b. The depth profiles of c) SIMS and d) LIBS for tile 8 sample 2ONG8B_11b and nearby sample 2ONG8B_10a. The co-deposited layer edge is defined by the falling Be signal for all of these depth profiles even though a) can fulfill the 50 % rising W signal condition. LIBS data is smoothed with a moving median over b) 7, d) 9 shots for improved visualization.

a nearby sample 14IWG1A_10a, located approximately 2 cm from sample 11a towards tile 3. The primary difference between the LIBS and SIMS profiles is caused by the change in the ablation rate at the W layer boundary (further discussed in section 3.5). It should be noted that the depth resolution of LIBS is much worse than with SIMS due to the ablation thickness and this complicates direct comparison between the methods. All of the ablated material contributes to the registered LIBS signal.

The mixed W layer: tile 3 (inner divertor), 7 (outer divertor) and 8 (outer divertor)

These samples were taken from the lower inner divertor (Fig. 9a and Fig. 9b) and the outer divertor (Fig. 9c and Fig. 9d) tiles. The three analyzed outer divertor samples had very similar depth profiles. A peculiarity common to the inner and outer divertor tiles was the lack of a clear W layer boundary (except for tile 3 SIMS), although these tiles also consisted of W-coated CFC. On the other hand, a relatively strong W signal persisted from the first laser shots, and the Mo layer boundary was well-defined. On tile 3, it took 14–18 shots to ablate through the co-deposited layer based on the falling signal of Be, while 4–10 shots were required for the samples from the outer divertor.

For LIBS samples from tile 3 and tile 8, the SIMS data was available only for nearby samples. The LIBS and SIMS depth profiles showed minor discrepancies along the depth axis, likely due to differences in the LIBS ablation rates or variations in the surface of nearby locations. Although the SIMS depth profile fulfills the condition of a rising W signal, the layer boundary is determined by the falling Be signal for the sake of comparison with LIBS. Another factor contributing to these discrepancies is the Gaussian laser beam profile, which allows signals from the surface layer to persist even when the center of the beam has reached the next layer.

Summary of LIBS and SIMS comparison

In the inner divertor, there was a trend of increasing co-deposited layer thicknesses and crater-to-crater variation (section 3.6) with height towards tile 0 (Fig. 10), similarly to earlier results [29]. Note that the error bars represent the range of layer thicknesses estimated by the number of LIBS shots required to ablate through the co-deposited layer. At the bottom of the divertor with the W lamella of tile 5, the co-deposited layer was ablated with 1–2 shots, while at the top of the inner divertor, the sample from HFGC required 600–870 shots for the ablation of the co-deposited layer. Additionally, the outer divertor had no clearly defined W layer. These observations align with findings from previous studies [2]. However, it should be noted that the 2ONG7A and 2ONG8B samples were exposed only during two ILW campaigns (ILW 2–3), and 2IWG3A during a single campaign (ILW 3). Furthermore, during the *in-situ* JET LIBS campaign, the co-deposited layers in the net deposition zone were potentially thicker since the LIBS campaign in JET covered tiles and components spanning throughout the entire ILW project lifetime (2011–2023).

LIBS demonstrated relatively poor depth resolution for very thin co-deposited layers, and the limited depth range of SIMS restricted direct comparison with the LIBS results for very thick co-deposited layers. For samples with intermediate layer thicknesses, SIMS qualitatively confirmed LIBS findings, similarly to earlier studies [29,35].

It is important to consider that multiple known and unknown variables influence the results, making direct, one-to-one comparisons between LIBS and SIMS data unfeasible, especially as neither method was calibrated. For instance, these unknown variables include the LIBS plasma parameters (electron density and temperature) and varying

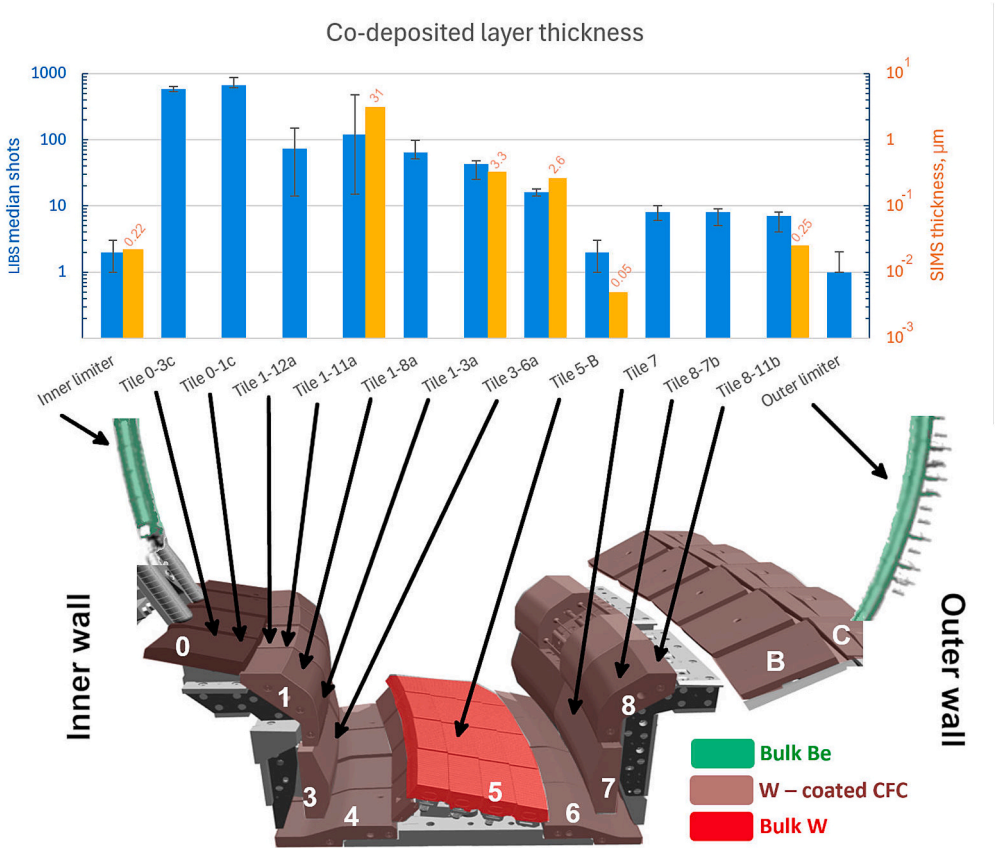

Fig. 10. The median number of laser shots required to ablate through the co-deposited layers in samples from different parts of the divertor along the poloidal direction. This is complemented by the SIMS estimates for the co-deposited layer thicknesses. The error bars indicate the range of required laser shots to ablate through the co-deposited layer at different spots on the same sample. Note the logarithmic scales.

ablation rates between sample layers, as discussed in section 3.5. Despite these limitations, the comparison provides a useful estimate of the resolution and accuracy of LIBS for determining elemental composition and depth profiles in the JET wall samples without prior calibration.

3.5. Ablation rate

Extra craters (craters 6+, Fig. 4) with varying depths (e.g., 1, 5, 10, 20, 50, 100 shots) were created on each sample to measure the ablation rates of the co-deposited and bulk layers using optical profilometry. These samples were analyzed at the National Institute for Laser, Plasma and Radiation Physics in Romania. The profilometry results showed high uncertainty due to rough sample surfaces and the inherent nature of the LIBS ablation process, as illustrated in Fig. 11. While only the limiter samples exhibited well-defined craters in the profilometry data, some usable data was extracted from other samples to compare ablation rates with the results presented in section 3.4.

As a trend, the ablation rate was at least twice as high in the bulk Be layer in the limiter tiles compared to the ablation rate in the divertor tiles with the W layer. The ablation rate of bulk material generally ranged between 100–140 nm/shot for limiter tiles (Be), while for the divertor tiles (W), it was around 30–50 nm/shot.

Similarly to the bulk of the limiter samples, the co-deposited layers predominantly consisted of Be, although most likely with a different material structure. The ablation rate of the co-deposited layers was consistently higher than in the W layers by a factor of 1.1–1.9. These findings are consistent with ablation rate estimates derived from the comparison of LIBS and SIMS depth profiles, with the ablation rate shifting from ~80 nm/shot in the co-deposited layer to ~40 nm/shot in the underlying W layer (Fig. 8c and Fig. 8d). It's not known why the ablation rate of the co-deposited layer is lower than that of the bulk Be in limiters, but a possible explanation could also be the relatively high uncertainty from the measurements.

3.6. Signal variation

This section analyzes shot-to-shot variation in LIBS line intensity and the variation of the signal of a given element (summed across multiple lines) within the co-deposited layer. Later, the crater-to-crater signal variation of an element in the co-deposited layer is discussed. The shot-to-shot and crater-to-crater analysis used shots 20–300 of the sample HFGC_1c (Fig. 7d) across six different craters. The first 20 shots were excluded due to trace element signals being higher and less uniform near the surface than deeper in the co-deposited layer. Finally, crater-to-crater variation in co-deposited layer thickness on the same sample is analyzed for different samples. Each analysis includes the uncertainties carried forward from the previous steps.

To evaluate shot-to-shot variation for strong elemental lines in a material with uniform composition, which is attributed to the variation of laser energy fluctuations, a pure Al sample (bulk Al, no JET plasma exposure) was analyzed. The shot-to-shot fluctuation of the signal had a coefficient of variation of 7 %. Similarly, the Ar signal arising from the breakdown of the ambient gas in the measurements of the JET samples showed a coefficient of variation of 8 %.

The shot-to-shot variation for elements within the co-deposited layer indicates the uniformity of material distribution throughout the layer depth. The intensities corresponding to the same shot number of different craters were averaged and then the standard deviation was found over all shot numbers. The coefficient of variation for signal fluctuation in the co-deposited layer was 11 % for Be, 25 % for Ni, and 25 % for hydrogen isotopes, while the baseline variation was 7 % (pure Al). W, Mo, and trace Inconel elements (Fe and Cr) were excluded from the analysis due to their signals being near the noise level, which would give the main contribution to the variation.

The crater-to-crater signal variation was analyzed for nearby craters (1–5 mm apart) on the same sample. The coefficients of variation were as follows: 15 % for Ni, 15 % for hydrogen isotopes, 16 % for Be, 17 % for Fe, 19 % for Cr, 21 % for Mo, and 23 % for W, compared to the baseline variation of 7 % (pure Al). Six depth profiles from craters made with the same experimental conditions were used to obtain these results and the depth profiles were smoothed using a moving average (7 shots) to minimize the shot-to-shot variation effect. Then the standard deviation of intensities corresponding to the same shot number of different craters was found and the average of the resulting 280 standard deviations (shots 20–300) was calculated. This was repeated for average intensities. Finally, the coefficient of variation was calculated as the average standard deviation divided by the mean intensity for each element. The crater-to-crater signal variation is also influenced by the thickness of the co-deposited layer, which is discussed later in this section.

These coefficients of variation provide insights into the homogeneity of the co-deposited layer in plasma-facing components. Shot-to-shot signal variation within a single crater was comparable to signal variation within nearby craters (up to 5 mm apart). Based on the coefficients of variation, the typical signal variation can be expected to be around 30 %, assuming consistent co-deposited layer thicknesses across locations on the sample.

When comparing layer thicknesses of nearby craters, uncertainty arises from both the LIBS signal and the co-deposited layer composition variation, as discussed earlier. However, these factors alone cannot explain variations in the layer thicknesses when the signal of the next layer emerges sharply over only a few shots. In such cases, the differences in the layer thicknesses are likely caused by spatially uneven erosion and re-deposition of material, leading to variations in both the layer thicknesses and the ablation rate of LIBS.

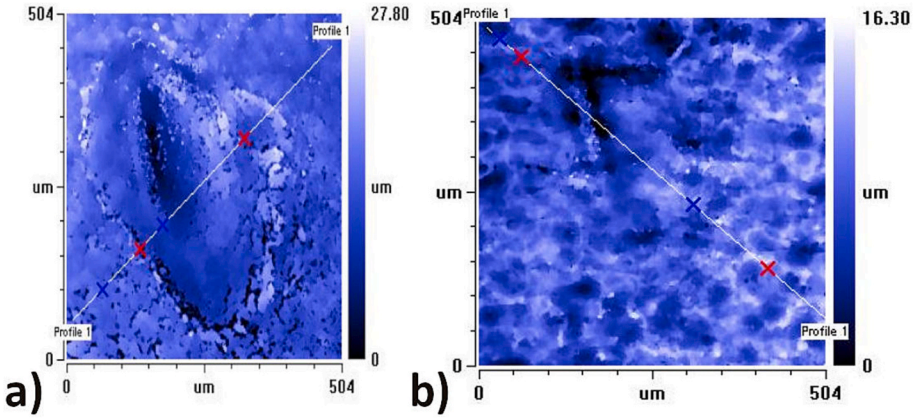

Fig. 11. Examples of profilometry results of a) 2XR11_668 limiter tile crater and b) B12_167 tile 5 crater. Both craters were created with 100 laser shots. The tile 5 sample crater is difficult to distinguish visually due to surface roughness and a lower ablation rate.

In the analyzed samples, even those with thick co-deposited layers, some cases showed clearly defined layer boundaries (±5 shots). In contrast, some cases exhibited a slow and fluctuating rise of the next layer signal (±100 shots). Crater-to-crater variation in layer thickness generally exceeded the uncertainty in estimating the layer boundary. The smallest variation (1–2 shots) was observed for the W lamella on tile 5 and the Be limiters, while the largest variation (15–480 shots or coefficient of variation of 100 %) occurred in the "apron", the horizontal part of tile 1. These findings suggest that areas dominated by erosion have so thin co-deposited layers that LIBS gives no noticeable local variation in the thickness of the layer. Conversely, areas dominated by deposition show significant local variations in the co-deposited layer thickness and/or the ablation rate as shown in earlier papers [24,34]. Outside of the "apron" the coefficients of variation of the layer thickness ranged between 10–40 %.

4. Summary

A LIBS experimental campaign was conducted at VTT to prepare for the *in-situ* LIBS campaign carried out at JET in 2024. The study established optimal experimental conditions with LIBS for JET and tested the prototype LIBS enclosure. The optimal conditions included a gate width of 1000 ns, balancing temporal resolution and signal strength, and a delay time of 1000 ns, chosen as a compromise between signal strength, line width, and compatibility with CF-LIBS requirements for future studies. The compact LIBS enclosure, equipped with a 20-meter optical fiber, attenuated signals below 300 nm, indicating the need for adjustments to the optics to detect C and, in the reactors with W first wall, B lines characterizing the boronization.

LIBS depth profiles were acquired for JET samples from the 2011–2016 campaigns at various locations across the reactor wall, focusing on the co-deposited layers in the divertor. The depth profiles clearly distinguished the different layers in the samples. Most divertor samples contained a co-deposited layer (primarily Be with other trace elements), followed by W, Mo, and CFC layers. The LIBS depth profiles qualitatively agreed with SIMS measurements despite neither method being calibrated. There were some discrepancies in the depth profiles on the depth axis, however, the differences were attributed to variations in the ablation rates across different layers and to the variation in deposition over a given tile.

The co-deposited layer thicknesses increased with height in the inner divertor when moving from tile 5 towards tile 0. On bulk Be limiters and stack B of tile 5 at the bottom of the divertor, the co-deposited layers were ablated through with 1–2 laser shots (50–300 nm), while the thickest layer on tile 0 at the top of the inner divertor required 870 shots (up to 120 μm) for ablation.

Ablation rates, estimated by the comparison of LIBS and SIMS depth profiles and optical profilometry, showed qualitative agreement. The bulk Be limiter tiles exhibited an ablation rate of ~100–140 nm/shot, while the W layers in other samples had rates of ~30–50 nm/shot. The ablation rate in the co-deposited layers (primarily Be) was up to twice as high as in the bulk W layers.

Signal and layer thickness variations were also investigated. With a homogeneous reference sample, the shot-to-shot variation of the LIBS signal was 7 %. Shot-to-shot and crater-to-crater LIBS signal variations were ~30 % for the JET samples. The variation in the thickness of the co-deposited layer was higher, likely due to the spatial characteristics of the deposition. The largest variation in nearby locations was observed on the top part of tile 1 ("apron"), where the ablating through of the co-deposited layer required 15 shots in one location and 480 shots just a few millimeters away. Typically, the variation in the layer thicknesses ranged between 10–40 %.

The study demonstrated that the compact LIBS enclosure and its optical configuration are suitable for measuring the depth profiles in JET. Despite the signal attenuation at lower wavelengths due to the optics, sufficient information was available for analysis. While hydrogen isotope lines could not be separated with the current Aryelle spectrometer, this issue was solved during the JET campaign by adding a high-resolution Littrow spectrometer to another fiber output.

Declaration of Generative AI and AI-assisted technologies in the writing process

During the preparation of this work, the authors used ChatGPT-4o (2025.04) under careful oversight to improve grammar and readability and nothing else. After using this tool, the authors reviewed and edited the content as needed and take full responsibility for the content of the published article.

CRediT authorship contribution statement

Jasper Ristkok: Writing – review & editing, Writing – original draft, Visualization, Investigation, Formal analysis. **Salvatore Almaviva:** Methodology, Investigation, Formal analysis, Conceptualization. **Jari Likonen:** Writing – review & editing, Visualization, Supervision, Resources, Project administration, Methodology, Investigation, Funding acquisition, Formal analysis, Conceptualization. **Juuso Karhunen:** Writing – review & editing, Methodology, Investigation. **Indrek Jõgi:** Writing – review & editing, Supervision, Investigation. **Peeter Paris:** Writing – review & editing, Supervision. **Shweta Soni:** Writing – review & editing, Investigation, Formal analysis. **Pavel Veis:** Writing – review & editing, Supervision. **Sahithya Atikukke:** Investigation. **Jelena Butikova:** Writing – review & editing, Investigation. **Rongxing Yi:** Investigation. **Ionut Jepu:** Writing – review & editing, Visualization, Resources, Investigation. **Pawel Gasior:** Writing – review & editing, Investigation. **Corneliu Porosnicu:** Investigation, Formal analysis. **Mihaela Bojan:** Investigation. **Bianca Solomonea:** Investigation. **Sebastijan Brezinsek:** Funding acquisition.

Declaration of competing interest

The authors declare that they have no known competing financial interests or personal relationships that could have appeared to influence the work reported in this paper.

Acknowledgements

This work has been carried out within the framework of the EUROfusion Consortium, partially funded by the European Union via the Euratom Research and Training Programme (Grant Agreement No 101052200 — EUROfusion). The Swiss contribution to this work has been funded by the Swiss State Secretariat for Education, Research and Innovation (SERI). Views and opinions expressed are however those of the author(s) only and do not necessarily reflect those of the European Union, the European Commission or SERI. Neither the European Union nor the European Commission nor SERI can be held responsible for them.

Data availability

Data will be made available on request.

References

[1] R. Aymar, P. Barabaschi, Y. Shimomura, The ITER design, Plasma Phys. Control. Fusion 44 (2002) 519–565, https://doi.org/10.1088/0741-3335/44/5/304.
[2] S. Krat, M. Mayer, A. Baron-Wiechec, S. Brezinsek, P. Coad, Y. Gasparyan, K. Heinola, I. Jepu, J. Likonen, P. Petersson, C. Ruset, G. De Saint-Aubin, A. Widdowson, Jet Contributors, Comparison of erosion and deposition in JET divertor during the first three ITER-like wall campaigns, Phys. Scr. T171 (2020) 014059, https://doi.org/10.1088/1402-4896/ab5c11.
[3] S. Krat, M. Mayer, J.P. Coad, C.P. Lungu, K. Heinola, A. Baron-Wiechec, I. Jepu, A. Widdowson, Comparison of JET inner wall erosion in the first three ITER-like

wall campaigns, Nucl. Mater. Energy 29 (2021) 101072, https://doi.org/10.1016/j.nme.2021.101072.
[4] J. Roth, E. Tsitrone, A. Loarte, Th. Loarer, G. Counsell, R. Neu, V. Philipps, S. Brezinsek, M. Lehnen, P. Coad, Ch. Grisolia, K. Schmid, K. Krieger, A. Kallenbach, B. Lipschultz, R. Doerner, R. Causey, V. Alimov, W. Shu, O. Ogorodnikova, A. Kirschner, G. Federici, A. Kukushkin, Recent analysis of key plasma wall interactions issues for ITER, J. Nucl. Mater. 390–391 (2009) 1–9, https://doi.org/10.1016/j.jnucmat.2009.01.037.
[5] D.A. Cremers, L.J. Radziemski, Handbook of Laser-Induced Breakdown Spectroscopy, 1st ed., Wiley, 2006. https://doi.org/10.1002/0470093013.
[6] V. Philipps, A. Malaquias, A. Hakola, J. Karhunen, G. Maddaluno, S. Almaviva, L. Caneve, F. Colao, E. Fortuna, P. Gasior, M. Kubkowska, A. Czarnecka, M. Laan, A. Lissovski, P. Paris, H.J. Van Der Meiden, P. Petersson, M. Rubel, A. Huber, M. Zlobinski, B. Schweer, N. Gierse, Q. Xiao, G. Sergienko, Development of laser-based techniques for in situ characterization of the first wall in ITER and future fusion devices, Nucl. Fusion 53 (2013) 093002, https://doi.org/10.1088/0029-5515/53/9/093002.
[7] H.J. Van Der Meiden, S. Almaviva, J. Butikova, V. Dwivedi, P. Gasior, W. Gromelski, A. Hakola, X. Jiang, I. Jõgi, J. Karhunen, M. Kubkowska, M. Laan, G. Maddaluno, A. Marín-Roldán, P. Paris, K. Piip, M. Pisarčík, G. Sergienko, M. Veis, P. Veis, S. Brezinsek, T. EUROfusion Wp Pfc Team, Monitoring of tritium and impurities in the first wall of fusion devices using a LIBS based diagnostic, Nucl. Fusion 61 (2021) 125001, https://doi.org/10.1088/1741-4326/ac31d6.
[8] A. Favre, A. Bultel, M. Payet, S. Vartanian, S. Garcia-Argote, V. Morel, E. Bernard, S. Markelj, M. Čekada, E. Hodille, A. Semerok, C. Grisolia, LIBS analysis of tritium in thin film-type samples, J. Nucl. Mater. 591 (2024) 154924, https://doi.org/10.1016/j.jnucmat.2024.154924.
[9] A. Ciucci, M. Corsi, V. Palleschi, S. Rastelli, A. Salvetti, E. Tognoni, New Procedure for quantitative elemental analysis by laser-induced plasma spectroscopy, Appl. Spectrosc. 53 (1999) 960–964, https://doi.org/10.1366/0003702991947612.
[10] E. Tognoni, G. Cristoforetti, S. Legnaioli, V. Palleschi, A. Salvetti, M. Mueller, U. Panne, I. Gornushkin, A numerical study of expected accuracy and precision in Calibration-Free Laser-Induced Breakdown Spectroscopy in the assumption of ideal analytical plasma, Spectrochim. Acta B At. Spectrosc. 62 (2007) 1287–1302, https://doi.org/10.1016/j.sab.2007.10.005.
[11] A. Favre, A. Bultel, M. Lamine Sankhe, S. Vartanian, V. Bruno, V. Morel, D. L'Hermite, J.-B. Sirven, M. Diez, M. Missirlian, P. Magaud, C. Grisolia, A step towards the diagnostic of the ITER first wall: in-situ LIBS measurements in the WEST tokamak, Phys. Scr. 99 (2024) 035609, https://doi.org/10.1088/1402-4896/ad2826.
[12] Z. Hu, X. Bai, H. Wu, R. Hai, F. Ding, M. Imran, C. Li, H. Ding, G.-N. Luo, Quantitative analysis of impurities deposited on the Plasma-Facing Components of EAST tokamak using a portable LIBS device, Nucl. Mater. Energy 41 (2024) 101785, https://doi.org/10.1016/j.nme.2024.101785.
[13] S. Almaviva, L. Caneve, F. Colao, G. Maddaluno, R. Fantoni, Accessory laboratory measurements to support quantification of hydrogen isotopes by in-situ LIBS from a robotic arm inside a fusion vessel, Spectrochim. Acta B At. Spectrosc. 181 (2021) 106230, https://doi.org/10.1016/j.sab.2021.106230.
[14] S. Almaviva, L. Caneve, F. Colao, V. Lazic, G. Maddaluno, P. Mosetti, A. Palucci, A. Reale, P. Gasior, W. Gromelski, M. Kubkowska, LIBS measurements inside the FTU vacuum vessel by using a robotic arm, Fusion Eng. Des. 169 (2021) 112638, https://doi.org/10.1016/j.fusengdes.2021.112638.
[15] Q. Xiao, R. Hai, H. Ding, A. Huber, V. Philipps, N. Gierse, G. Sergienko, In-situ analysis of the first wall by laser-induced breakdown spectroscopy in the TEXTOR tokamak: dependence on the magnetic field strength, J. Nucl. Mater. 463 (2015) 911–914, https://doi.org/10.1016/j.jnucmat.2014.10.065.
[16] S.S. Harilal, A.K. Shaik, E.J. Kautz, A. Devaraj, A.M. Casella, D.J. Senor, Detection of tritium using ultrafast laser-induced breakdown spectroscopy, J. Anal. At. Spectrom 39 (2024) 699–703, https://doi.org/10.1039/D3JA00439B.
[17] R. Skilton, N. Hamilton, R. Howell, C. Lamb, J. Rodriguez, MASCOT 6: Achieving high dexterity tele-manipulation with a modern architectural design for fusion remote maintenance, Fusion Eng. Des. 136 (2018) 575–578, https://doi.org/10.1016/j.fusengdes.2018.03.026.
[18] B.N. Chichkov, C. Momma, S. Nolte, F. Alvensleben, A. Tünnermann, Femtosecond, picosecond and nanosecond laser ablation of solids, Appl. Phys. A 63 (1996) 109–115, https://doi.org/10.1007/BF01567637.
[19] P. Paris, J. Butikova, M. Laan, A. Hakola, I. Jõgi, J. Likonen, E. Grigore, C. Ruset, Comparison of LIBS results on ITER-relevant samples obtained by nanosecond and picosecond lasers, Nucl. Mater. Energy 18 (2019) 1–5, https://doi.org/10.1016/j.nme.2018.11.018.
[20] I. Jõgi, J. Ristkok, J. Butikova, J. Raud, P. Paris, LIBS plasma in atmospheric pressure argon, nitrogen and helium: spatio-temporal distribution of plume emission and Hα linewidth, Nucl. Mater. Energy 37 (2023) 101543, https://doi.org/10.1016/j.nme.2023.101543.
[21] I. Jõgi, J. Ristkok, J. Raud, J. Butikova, K. Mizohata, P. Paris, Laser induced breakdown spectroscopy for hydrogen detection in molybdenum at atmospheric pressure mixtures of argon and nitrogen, Fusion Eng. Des. 179 (2022) 113131, https://doi.org/10.1016/j.fusengdes.2022.113131.
[22] S.S. Harilal, G.V. Miloshevsky, P.K. Diwakar, N.L. LaHaye, A. Hassanein, Experimental and computational study of complex shockwave dynamics in laser ablation plumes in argon atmosphere, Phys. Plasmas 19 (2012) 083504, https://doi.org/10.1063/1.4745867.
[23] A. Lahtinen, J. Likonen, S. Koivuranta, E. Alves, A. Baron-Wiechec, N. Catarino, J. P. Coad, K. Heinola, J. Räisänen, A. Widdowson, Deuterium retention on the tungsten-coated divertor tiles of JET ITER-like wall in 2015–2016 campaign, Fusion Eng. Des. 146 (2019) 1979–1982, https://doi.org/10.1016/j.fusengdes.2019.03.081.
[24] A. Baron-Wiechec, A. Widdowson, E. Alves, C.F. Ayres, N.P. Barradas, S. Brezinsek, J.P. Coad, N. Catarino, K. Heinola, J. Likonen, G.F. Matthews, M. Mayer, P. Petersson, M. Rubel, W. Van Renterghem, I. Uytdenhouwen, Global erosion and deposition patterns in JET with the ITER-like wall, J. Nucl. Mater. 463 (2015) 157–161, https://doi.org/10.1016/j.jnucmat.2015.01.038.
[25] M. Wojdyr, Fityk: a general-purpose peak fitting program, J. Appl. Crystallogr. 43 (2010) 1126–1128, https://doi.org/10.1107/S0021889810030499.
[26] P. Yaroshchyk, J.E. Eberhardt, Automatic correction of continuum background in Laser-induced Breakdown Spectroscopy using a model-free algorithm, Spectrochim. Acta B At. Spectrosc. 99 (2014) 138–149, https://doi.org/10.1016/j.sab.2014.06.020.
[27] A. Kramida, Y. Ralchenko, J. Reader, NIST ASD Team, NIST Atomic Spectra Database (version 5.12), NIST Standard Reference Database 78, (2024). Available: https://physics.nist.gov/asd (accessed 29.12.2024). https://doi.org/10.18434/T4W30F.
[28] R.L. Kurucz, B. Bell, Atomic spectral line database from CD-ROM 23 of R. L. Kurucz, (1995). Available: https://lweb.cfa.harvard.edu/amp/ampdata/kurucz23/sekur.html (accessed 29.12.2024).
[29] J. Karhunen, A. Hakola, J. Likonen, A. Lissovski, M. Laan, P. Paris, Applicability of LIBS for in situ monitoring of deposition and retention on the ITER-like wall of JET – comparison to SIMS, J. Nucl. Mater. 463 (2015) 931–935, https://doi.org/10.1016/j.jnucmat.2014.10.028.
[30] S.A. Puyang, Y.P. Xu, Y.H. Guan, Z.S. Yang, F. Ding, H.S. Zhou, G.Z. Zuo, J.S. Hu, G.-N. Luo, the EAST Team, Evolution of hydrogen isotopes retention behavior of in-situ boronization films in EAST, Nucl. Fusion 64 (2024) 074001, https://doi.org/10.1088/1741-4326/ad4897.
[31] P. Kumar, S. Soumyashree, N. Rao Epuru, S.B. Banerjee, R.P. Singh, K. P. Subramanian, Determination of stark shifts and widths using time resolved laser-induced breakdown spectroscopy (LIBS) measurements, Appl. Spectrosc. 74 (2020) 913–920, https://doi.org/10.1177/0003702819891172.
[32] G. Cristoforetti, A. De Giacomo, M. Dell'Aglio, S. Legnaioli, E. Tognoni, V. Palleschi, N. Omenetto, Local thermodynamic equilibrium in laser-induced breakdown spectroscopy: beyond the McWhirter criterion, Spectrochim. Acta B At. Spectrosc. 65 (2010) 86–95, https://doi.org/10.1016/j.sab.2009.11.005.
[33] G. Shaw, M. Bannister, T.M. Biewer, M.Z. Martin, F. Meyer, B.D. Wirth, The detection of He in tungsten following ion implantation by laser-induced breakdown spectroscopy, Appl. Surf. Sci. 427 (2018) 695–703, https://doi.org/10.1016/j.apsusc.2017.08.180.
[34] M. Mayer, S. Krat, W. Van Renterghem, A. Baron-Wiechec, S. Brezinsek, I. Bykov, P. Coad, Y. Gasparyan, K. Heinola, J. Likonen, A. Pisarev, C. Ruset, G. De Saint-Aubin, A. Widdowson, J.E.T. Contributors, Erosion and deposition in the JET divertor during the first ILW campaign, Phys. Scr. T167 (2016) 014051, https://doi.org/10.1088/0031-8949/T167/1/014051.
[35] P. Veis, A. Marín-Roldán, V. Dwivedi, J. Karhunen, P. Paris, I. Jõgi, C. Porosnicu, C. P. Lungu, V. Nemanic, A. Hakola, Quantification of H/D content in Be/W mixtures coatings by CF-LIBS, Phys. Scr. 2020 (2020) 014073, https://doi.org/10.1088/1402-4896/ab7ebd.